Developments in Synchrotron X-Ray Microtomography for Application to Flow in Porous Media

R. D. Hazlett[1], M. E. Coles[1], K. W. Jones[2], B. Andrews[2], B. Dowd[2], P. Siddons[2], and A. Peskin[2]

Abstract

Microimaging capabilities at Brookhaven National Laboratory's National Synchrotron Light Source have been enhanced to provide larger and higher resolution 3-D renderings of pore networks in reservoir rocks at a fraction of the time required in previous first generation scanning methods. Computer Microtomography, CMT, volumes containing 16 million voxels have been acquired at 3 micron resolution with the aid of expansion optics in a matter of hours. Such data are used to model single and multiphase flow properties in digital images of real porous media. Advances in 3-D visualization, which are being implemented in Brookhaven National Laboratory's 3-D theater, will allow even greater digestion and interpretation of phenomena dependent upon pore interconnectivity and multipore interactions. Pore networks are analyzed for tortuosity and connectivity measures, which have been elusive parameters in transport property models. We present examples of porosimetry simulation via network modeling to produce initial water saturation and residual oil distributions in a water-wet pore system. Furthermore, pore networks can provide the boundary condition framework for more rigorous simulations of displacement, such as in the lattice Boltzmann simulated water flood example provided.

Introduction

Computed Microtomography (CMT) has been available at the National Synchrotron Light Source (NSLS) at Brookhaven National Laboratory for many years[1-8]. First generation scanning methods gave high resolution images of geological and biological samples approaching 1 μm resolution. First generation scanning provided necessary detail in moderate to high permeability porous media samples for transport property modeling with computational fluid dynamics methods[9-11]. The time requirements of first generation methods limited the number of samples which could be investigated and restricted the potential of in-situ experimental monitoring[12]. Implementation of array detection technology has enabled acquisition of larger 3-D volumes at a fraction of the time required in first generation scanning. Initial implementation, however, was limited by the resolution of fluorescing elements of the detector material, on the order of 10 μm rather than 1 μm. With the introduction of expansion optics, images of 2.7 μm resolution have been obtained containing in the neighborhood of $3x10^7$ voxels. Improvements in data acquisition, transmission, and reconstruction have reduced the time requirements to produce such a volume to a few hours. Herein we document the status of CMT at the NSLS and display a variety of applications using such data on reservoir rock samples.

Advances in Imaging

A schematic of the CMT apparatus is provided as Figure 1. X-ray CMT produces a cross-sectional map, or slice, of linear x-ray attenuation coefficients inside a small sample. To obtain the data for a reconstructed slice, the x-rays transmitted through a single slice of the sample are recorded on a linear array of detectors. The sample is rotated, with the axis of rotation perpendicular to the plane of the incident beam, by a discrete angular interval determined by the linear resolution desired. The transmission of each ray through the sample, along a line from the source to the detector is recorded; this represents a line integral of the attenuation coefficients along this ray. The procedure is repeated for each angular view until the sample has been rotated by 180° in the x-ray beam. The transmitted x-ray values recorded at each detector in the linear array, obtained for each view in the slice, are then processed using a filtered back-projection algorithm to reconstruct the horizontal slice.

[1]Mobil Exploration and Producing Technical Center, P.O. Box 819047, Dallas, TX 75381-9047.
[2]Brookhaven National Laboratory, Upton, NY 11973.

The CMT workstation at NSLS experimental beamline station X27C incorporates a cooled charge-coupled device (CCD) camera with 1317 x 1035 pixels, Kodakís KAF-1400 chip. Each row of pixels constitutes one linear detector array and provides the data to reconstruct one 2-D slice of the sample. Subsequently, the CCD records the data to reconstruct over 1000 horizontal slices, simultaneously. Instead of detecting x-ray transmission directly, which would limit the spatial resolution to the detector size, a thin high-resolution YAG scintillator placed behind the sample converts each x-ray attenuation map to a visible image, which is then magnified and re-imaged with conventional optics onto the cooled CCD area array.

The use of imaging optics allows the flexibility to make a simple lens change and view larger samples with lower magnification, as desired. To date, a continuously variable .75x to 3x lens, a 4x lens, and a 10x lens have been used to collect data from various samples, ranging in size from .5 to 12 mm. To protect the camera optics and detector array from direct exposure to x-rays, the camera is positioned at 90° to the incident beam. The visible image produced by the scintillator is then folded into the camera by a flat, disposable mirror, as shown in Figure 1.

All alignment stages for image acquisition are remotely controlled over a GPIB bus. Prior to collecting the images needed for reconstruction, the sample under examination is aligned to the field of view of the CCD using goniometer stages. These in turn are mounted on the rotation stage which is stepped during data collection. The axis of rotation must be coincident with the center column of pixels in the camera for proper implementation of the tomography reconstruction algorithm. Once the sample is aligned, an automated program is initiated to rotate the sample, take a snapshot of the visible impression of the attenuation map on the scintillator, at each viewing angle, and save each image for later reconstruction. Presently, the data collection is performed with a 386 PC. A user-friendly Visual Basic routine was written to access the motors for alignment and to automatically rotate the sample and grab and store images from the camera. The image files are then transferred to a Silicon Graphics Indigo for reconstruction and 3-D rendering. The setup is presently being upgraded to eliminate the PC and control both image acquisition and reconstruction from the Indigo.

The volumetric data can at this point be transferred via an Asynchronous Transfer Mode (ATM) link for display in a large screen stereo viewing room. The display system is driven by a Silicon Graphics Reality Station with a single CPU, single Reality Engine, and two Raster Manager Boards. Dual viewports are created with a Multi-Channel Option. The stereo effect is achieved through superposition of two full resolution, polarized images using rear projection onto a 10 foot screen, specially treated to retain light polarization. Stereo images are then viewed through simple polarized glasses. The system was designed for superior image quality, ease of replication, and high-speed network interaction so that visualization can occur at several locations simultaneously by collaborative teams. These advances in 3-D visualization allow enhanced digestion and interpretation shortly after CMT data acquisition.

A sample of a North Sea Brent sandstone acquired at 2.7 μm resolution is shown in Figure 2. We show a 3-D representation of the cylindrical volume with a wedge removed to reveal the interior. Given also in Figure 2 are interior orthogonal slices which reveal the extent of detail captured in this 470 md sample. These images demonstrate the ability of CMT to simultaneously capture intergranular porosity and elements of microporosity in a 3-D pore network. The sharpness of grain boundaries at this magnification attests to the quality of image data. We can certainly see variations in mineralogy and can begin to digest surface compositional information important for rock-fluid interactions, i.e. wettability.

Applications

Spatial Correlation

A number of researchers have made use of spatial correlation functions to describe, and indeed synthesize, pore networks. Such information provides significant compression of statistical detail, useful for correlating transport and rock properties. The necessity of such measures is real, but recent studies have cast doubt concerning the sufficiency of traditional spatial correlation functions in describing rock texture[13]. In that work, a new measure, the

extended variogram, was introduced to capture local variability information lost in the averaging procedure of the traditional variogram or autocorrelation function. An example of such an extended variogram computed from CMT data is shown in Figure 3. The extended variogram closely resembles the traditional variogram with error bars indicating the standard deviation of the distribution about the median variance. This approach recognizes that reservoir rocks contain pore size distributions and are not, in general, isotropic.

Connectivity

One of the first realizations after viewing 3-D porosity networks is that it is very difficult to determine what constitutes a pore. This has serious implications for pore size distribution determinations from 2-D image analysis. In CMT data, we observe what can be easily seen as distinct objects in a 2-D image as simply cross sections of interconnected void space. Cluster analysis in 3-D does not produce pore size distributions. Cluster analysis[13-15] can be a valuable tool to describe the size of independent blobs and diagnose the extent of connectivity. Percolation is, of course, mandatory for modeling fluid flow through the pore network. The rendering of pore throats dictates the resolution requirements in CMT for each of our rock specimens. Pore throat size information is most readily obtained from mercury intrusion and not from the images themselves without the aid of a segentation scheme, such as the one described in the network modeling section.

A successive erosion algorithm makes use of connectivity measures to determine the characteristic or critical pore throat size. In erosion[15], the surface layer of the pore system is removed. Each erosion removes two voxels from a pore diameter, one from each surface. Following an erosion cycle, a cluster analysis and percolation assessment are performed. Additional erosions are performed until the resulting network no longer percolates. This process defines the smallest pore throat in the pore space necessary for fluid transport to within 1 voxel. This characteristic length scale is strongly correlated to medium permeability[16] and should be correlated to individual phase permeabilities, should their spatial distributions be known. An example of the successive erosion technique applied to CMT data is shown in Figure 4. Individual clusters are shaded according to the number of voxels in each cluster, but connectivity information can easily be gathered from the continuity of color.

Tortuosity

A close relative of erosion, which helps to define a measure of medium tortuosity, is the skeletonization[15] process. In creating a pore network skeleton, erosion is performed with an additional check. No voxel is removed if it causes a disconnection. A skeletonization routine was written to process CMT pore networks. Comparable routines have been written elsewhere[17]. The skeleton represents a collapse of the pore network to a central axis network. Skeletons still contain dead ends. Of most interest is the skeleton backbone. The skeleton backbone represents more or less the centerline for flow across the pore system. Backbone images were derived from skeletons using a self-avoiding random walk procedure. A large number of walkers were introduced at one volume face on skeleton elements. Walkers were allowed to take steps along skeleton elements with a prescribed diffusion coefficient, e.g. one attempt per time step, but no walker was allowed to revisit sites. An image was constructed of all self-avoiding walks which were successful in reaching the other end of the model. Such an image represents all possible percolation pathways. An example is shown in Figure 5. From the number of time steps required to traverse the volume, the diffusion coefficient, and the volume dimensions, a tortuosity can be computed. Such a calculation for the backbone image in Figure 5 is provided in Figure 6 and yields an average tortuosity of 2.68. This value of tortuosity is in line with reported literature values for moderate to high permeability sandstones.

Network Modeling

Simulation of capillary dominated displacements is possible on arbitrarily complex CMT pore systems using percolation and network model concepts[10]. Details of the algorithms are not presented here, but the main ideas will be outlined. The model contains no dynamics, but computes saturation changes from one equilibrium state to another. It is possible to simulate any capillary pressure history within the framework of assumptions regarding wettability and

wetting alteration, enabling us to reproduce procedures such as the combined USBM-Amott test on CMT data sets[10].

Network model simulation is performed based upon a computation of all stable interfacial positions at prescribed capillary pressures and tests for phase continuity. An operating assumption is that the wetting phase always maintains connectivity, regardless of saturation. The nonwetting phase, however, must maintain continuity with a surface defined for mass transfer in order to move. In the simplest implementation, wettability is considered a binary property. In practice, it is the nonwetting phase occupation which is tracked and not the wetting phase or interfaces.

Primary drainage simulation proceeds as follows. For each voxel belonging to the pore space, the diameter of the largest inscribed sphere is computed. For example, those voxels adjacent to a wall will be assigned a value of 0.5. In such a manner, an inscribed sphere mask is produced. At a fixed capillary pressure and corresponding pore entry radius, the union of all spheres with radius greater than or equal to the pore entry radius is rendered. The actual nonwetting phase saturation distribution is that subset of sphere assemblages that is connected to a reservoir of nonwetting phase. Typically we deal with rectangular parallel piped data, and the user must define which exterior planes are in contact with the nonwetting fluid reservoir. The predicted phase distributions at each capillary pressure are labeled and stored as 3-D image arrays. Since fluid-fluid interfaces will reside at pore throats, the predicted equilibrium fluid distributions (and their associated interfaces) can be used to segment the pore space and identify "pores" and "throats". An example of primary drainage in a CMT volume is given in Figure 7 where the rock is gray, the nonwetting phase is black, and the wetting phase is white. Figure 7b is an example of computation of an initial water saturation image in preparation for a numerical flooding experiment.

Imbibition network model simulation is slightly more complex. A percolation-type approach is again used which assumes the wetting phase has no mechanistic barrier to transport anywhere in the network, whereas the nonwetting phase is divided into moveable and stranded fractions. It is also assumed that the prefered fluid configurations based upon interfacial curvature without regard to accessibility are identical in drainage and imbibition directions. In imbibition, a predicted nonwetting phase distribution is a combination of fluid already in the preferred equilibrium position, fluid trapped in prior steps, and fluid which will be trapped when the capillary pressure is further reduced. In practice, the nonwetting phase distribution is computed from a convoluted series of union and intersection operations involving the current state, primary drainage states, and the accessibility-independent fluid distributions which served as precursors in primary drainage simulation. The predicted residual oil distribution for the imbibition process starting with the initial water saturation image of Figure 7a is shown in Figure 7c.

Of course, for every 3-D fluid distribution, one could compute the macroscopic saturations to produce synthetic capillary pressure curves. This has been done for the 3-D CMT volume highlighted in experimental and numerical work of reference 12 and is provided in Figure 8. In this figure, we show the synthetic capillary pressure data along with mercury intrusion data, already reduced to pore entry size. The similarity in shape of the two curves is remarkable. The shift between sets of data could be the result of microporosity not captured in the CMT volume, error in thresholding the CMT data ($\pm$ 0.5 voxel, or in this case 15 μm) which is represented by the error bars on the network result, or uncertainty in the product of mercury-mercury vapor interfacial tension and cosine of the contact angle. Both sets of capillary pressure data indicate an extreme sensitivity between applied capillary pressure and saturation, a measure of pore throat uniformity for this sample.

Computational Fluid Dynamics

CMT data can serve as boundary conditions in modeling fluid transport[8-12]. Finite difference methods have proven useful for single phase calculations[8]. We have chosen the lattice Boltzmann method (LBM) to model fluid flow because of its ability as a computational fluid dynamics technique to perform multiphase simulation. The LBM used[18] was a variation of the model developed at Los Alamos National Laboratory (LANL) and customized for flow in

porous media in a collaborative effort between LANL and Mobil[11]. The model can handle any wettability distribution and yields accurate hydrodynamics provided that the flow conduit has a minimum of three lattice cells. This last restriction guides us in CMT data resolution specifications for reservoir rocks of interest. Although grid refinement or coarsening with CMT data is possible, in our simulation efforts, we have used a one-to-one correspondence between lattice cells and CMT image voxels.

Lattice Boltzmann simulation is well suited for massively parallel processing. Our simulations have typically been run on 128 nodes of a Thinking Machines CM-5 computer, using resources either at LANL or Mobil. The lattice Boltzmann variables have real world equivalents, including time. Thus, the slower the velocity (or Capillary Number, N_{Ca}) desired to simulate, the longer it takes to complete a displacement. Since we were primarily interested in low N_{Ca} floods, dynamic displacement simulations required tens of hours to complete for a typical 128^3 geometry.

The LBM has been used for both single and multiphase displacement simulations. Reasonable agreement has been found between permeabilities from simulation on CMT data and core plug measured values[11]. Excellent correlation has also been observed between phase distributions from physical displacement experiments monitored by CMT[12] or Magnetic Resonance Imaging[19] (MRI) and lattice Boltzmann numerical experiments. In some scenarios, numerical experiments are, in fact, easier to carry out. Snapshots from an example LBM simulated waterflood are provided in Figure 9. In this water-wet example, a low initial water saturation of approximately 12%, derived from network model simulation, served as the starting condition for the LBM displacement. In Figure 9, the rock has been made transparent so that only the pore space, filled either with oil (light) or water (dark), is visible. This particular displacement was carried out with N_{Ca} around 10^{-4}. Pressure and velocity information can be reported in addition to saturation so that relative permeabilities can be computed for each phase for either steady or unsteady state conditions.

Conclusions

Advances in CMT acquisition have occurred at the Brookhaven NSLS facility which allow greater access to larger high resolution volumes on more samples. These advances are a result of improved hardware, software, and technique. A large set of information useful in modeling properties of and processes in porous media can be gained from CMT data. A significant number of examples have been cited. We believe this avenue of research will lead to improved understanding of the physics of hydrocarbon recovery and can in the future provide the basis for transport property prediction from rock texture characteristics.

Acknowledgments

Collaborative work between BNL, Mobil, and GTE was sponsored by an ACTI grant from the DOE. The work was, in part, sponsored through U.S. DOE contract DEAC02-76CH00016. Special thanks go to M. Schlackman at GTE for his help in 3-D theater design. A portion of the lattice Boltzmann simulation work was performed using the resources located at the Advanced Computing Laboratory of Los Alamos National Laboratory, Los Alamos, NM 87545. Permission to publish from Mobil management is gratefully acknowledged.

References

1. Spanne, P. and Rivers, M. (1987) "Computerized Microtomography using Synchrotron Radiation from the NSLS," *Nucl. Instr. Meth. Phy. Res.*, 1063-67.
2. Nichols, M.C., Kinney, J. H., Johnson, Q.C., Saroyan, R.A., Bonse, U., Nusshardt, R., and Pahl, R. (1989) "Synchrotron Microtomography of Supported Catalysts," *Rev. Sci. Inst.*, **60**(7), 2475-77.
3. Jones, K.W., Spanne, P., Webb, S.W., Conner, W.C., Beyerlein, R.A., Reagan, W. J., and Dautzenberg, F.M. (1991) "Catalyst Analysis using Synchrotron X-ray Microscopy," *Nuc. Inst. Meth. Phy. Res.*, 427-432.
4. Conner, W.C., Webb, S.W., Spanne, P., and Jones, K.W. (1990) "Use of X-ray Microscopy and Synchrotron Microtomography to Characterize Polyethylene Polymerization Particles," *Macromolecules* **20**, 4742-47.

5. Flannery, B.P., Deckman, H.W., Roberge, W.G., and D'Amico, K.L., (1987) "Three Dimensional X-ray Microtomography," *Science* **237**(18 September), 1439-44.
6. Dunsmuir, J. H., Ferguson, S.R., D'Amico, K.L., and Stokes, J.P. (1991) "X-Ray Microtomography: A new Tool for the Characterization of Porous Media," SPE paper 22860, presented at the 66th Annual Technical Conference and Exhibition of the Society of Petroleum Engineers, Dallas, October 6-9.
7. Coles, M.E., Spanne, P., Muegge, E.L., and Jones, K.W. (1994) "Computed Microtomography of Reservoir Core Samples," SCA 9401, presented at the Society of Core Analysts Annual Technical Conference, September 12-14.
8. Spanne, P., Thovert, J.F., Jacquin, C.J., Lindquist, W.B., Jones, K.W., and Adler, P.M. (1994) "Synchrotron Computed Microtomography of Porous Media: Topology and Transports," *Physical Review Letters* **73**(14), 2001-2004.
9. Ferréol, B., and Rothman, D.H. (1995) "Lattice-Boltzmann Simulations of Flow Through Fontainebleau Sandstone," *Transport in Porous Media* **20**, 3-20.
10. Hazlett, R. D. (1995) "Simulation of Capillary-Dominated Displacements in Microtomographic Images of Reservoir Rocks," *Transport in Porous Media* **20**, 21-35.
11. Buckles, J.J., Hazlett, R.D., Chen, S.Y., Eggert, K.G., Grunau, D.W., and Soll, W.E. (1994) "Toward Improved Prediction of Reservoir Flow Performance," *Los Alamos Science*, n. 22, 112-121.
12. Coles, M.E., Hazlett, R.D., Spanne, P., Muegge, E.L., Soll, W.E., and Jones, K.W. (1996) "Pore Level Imaging of Fluid Transport using Synchrotron X-Ray Microtomography," SCA paper, presented at the Society of Core Analysts Annual Technical Conference, Montpellier, September 8-10.
13. Hazlett, R.D. "Statistical Characterization and Stochastic Modeling of Pore Networks in Relation to Fluid Flow," submitted to *Mathematical Geology*.
14. Hoshen, J., and Kopelman, R. (1976) "Percolation and Cluster Distribution. I. Cluster multiple labeling technique and critical concentration algorithm," *Physical Review B* **14**(8), 3438-3445.
15. Russ, J.C. (1992) The Image Processing Handbook, CRC Press: Boca Raton.
16. Katz, A.J., and Thompson, A.H. (1986) "Quantitative Prediction of Permeability in Porous Rocks," *Phys. Rev. B* **34**(11), 8179-8181.
17. Lindquist, W.B., Lee, S-M, Coker, D.A., Jones, K.W., and Spanne, P. (1996) "Medial Axis Analysis of Void Structure in Three Dimensional Tomographic Images of Porous Media," *Journal of Geophysical Research*, in press.
18. Grunau, D., Chen, S.Y., and Eggert, K.G. (1993) "A Lattice Boltzmann Model for Multiphase Fluid Flows," *Physics of Fluids A* **5**(10), 2557-2562.
19. Vaidya, R.N., Hazlett, R.D., Buckles, J.J., Coles, M.E., Grunau, D.W., Chen, S.Y., and Eggert, K.G. (1994) "Simulation of Wettability Effects on Displacement Processes by Cellular Automata Methods," presented at the Third International Symposium on Evaluation of Reservoir Wettabliity and its Effect on Oil Recovery, Laramie, September 21-23.

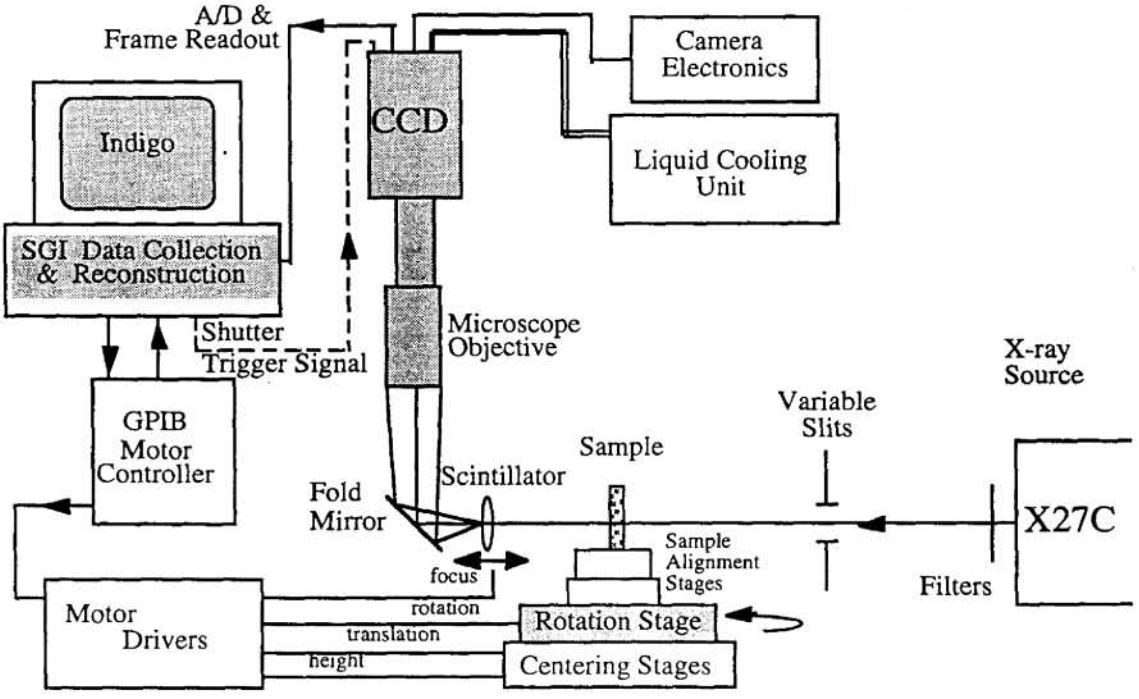

Figure 1. Brookhaven Synchrotron CMT apparatus.

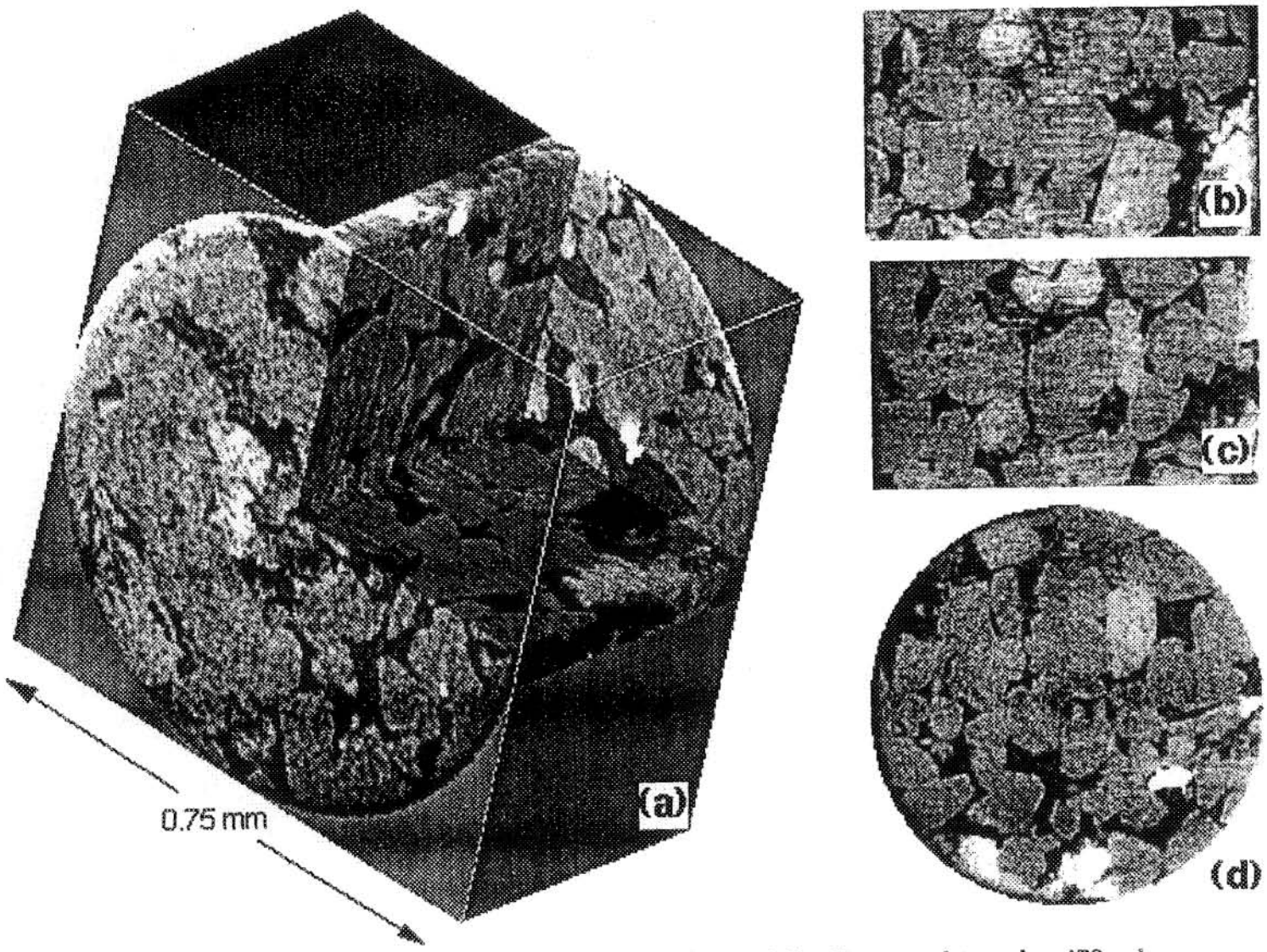

Figure 2. High resolution (2.7 micrometer) CMT subvolume of a North Sea Brent sandstone, k = 470 md: a) 3-D perspective with cutaway, b) X-directional slice, c) Y-directional slice, d) Cross section.

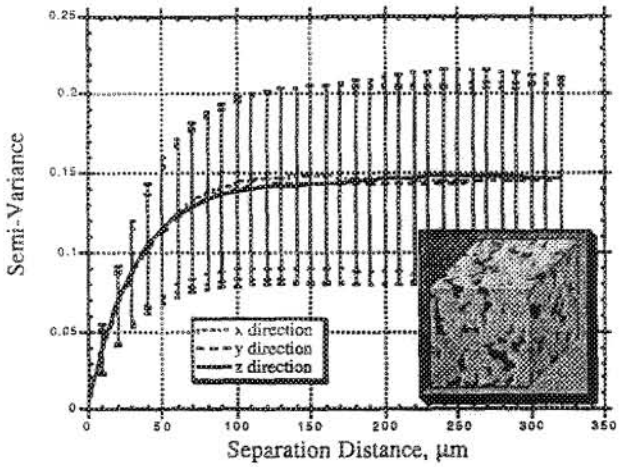

Figure 3. Extended variogram analysis for a 1100 md Berea sandstone CMT volume at 10 µm resolution.

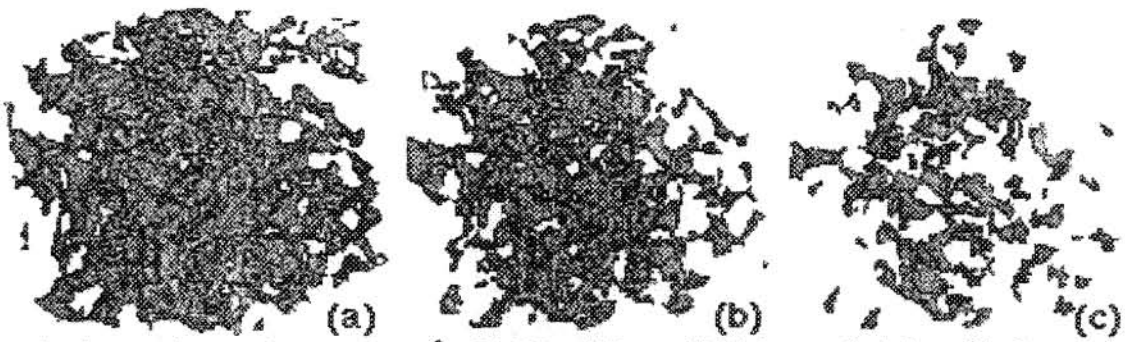

Figure 4. Successive erosions on 1 mm^3 of 1100 md Berea CMT data to find the critical pore throat radius for correlation to medium permeability: a). Interconnected pore space, b). Interconnected pore space, 1 erosion, c). Disconnected pore space, 2 erosions.

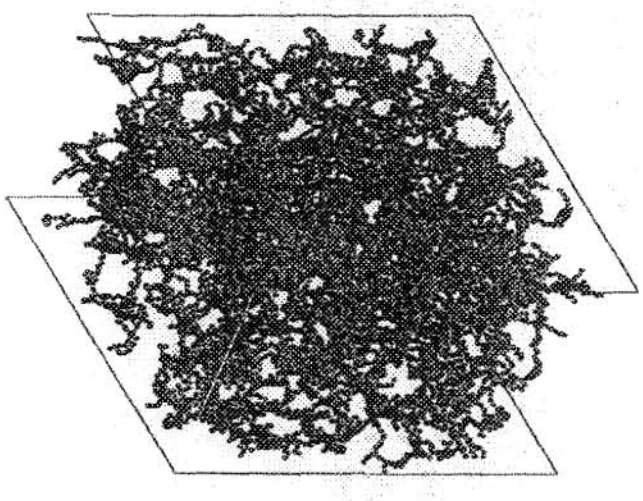

Figure 5. Map of successfully traversing self-avoiding walks on a CMT volume skeleton for a 15 darcy sandstone, thus defining the possible pathways for fluid flow.

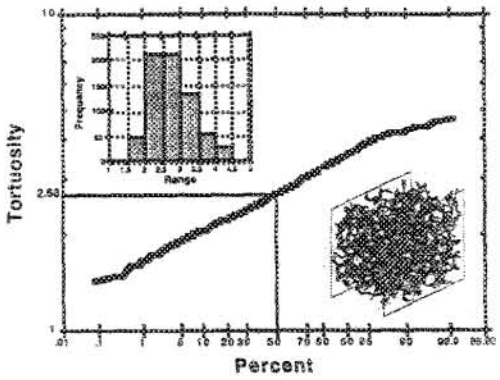

Figure 6. Tortuosity distribution for self-avoiding walk paths along the pore network skeleton backbone of Fig. 5, indicating a log normal distribution with a mean value of 2.68.

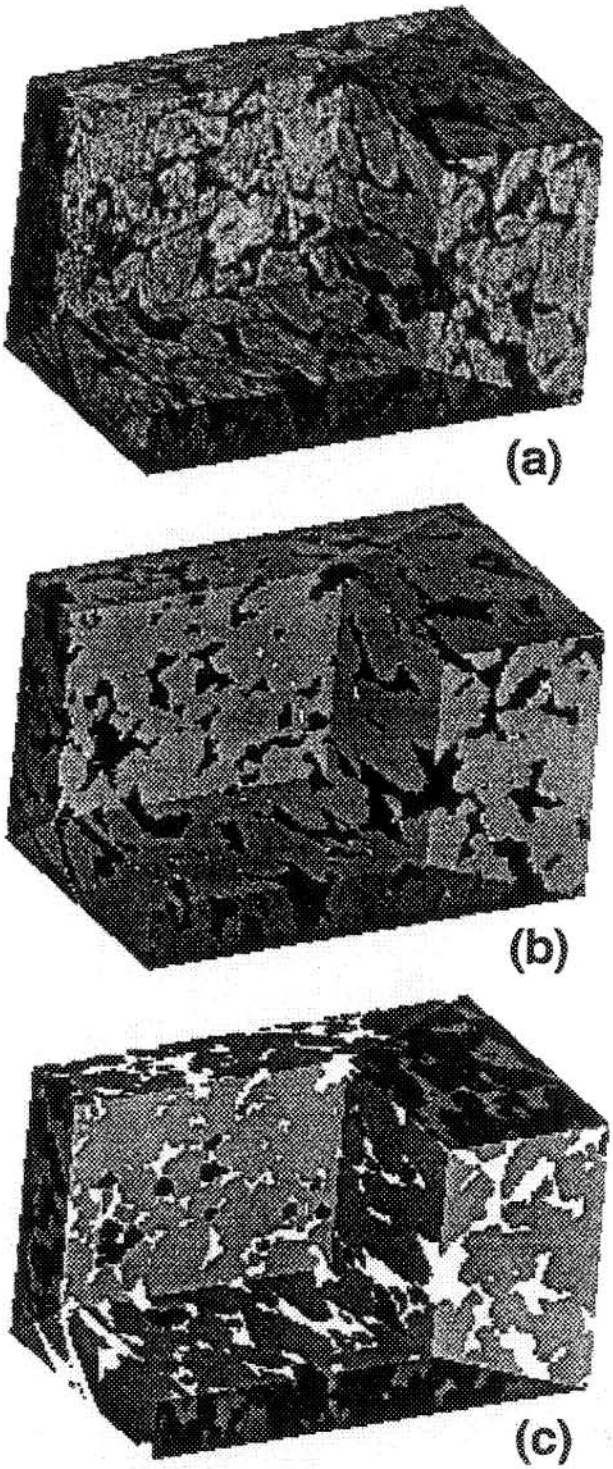

Figure 7. 3-D Cutaway images of a 5.8 darcy producing reservoir sandstone and network model predicted fluid distributions: a). CMT volume image, b). S_{iw} image, c). S_{or} image. Gray = rock; black = oil; white = water.

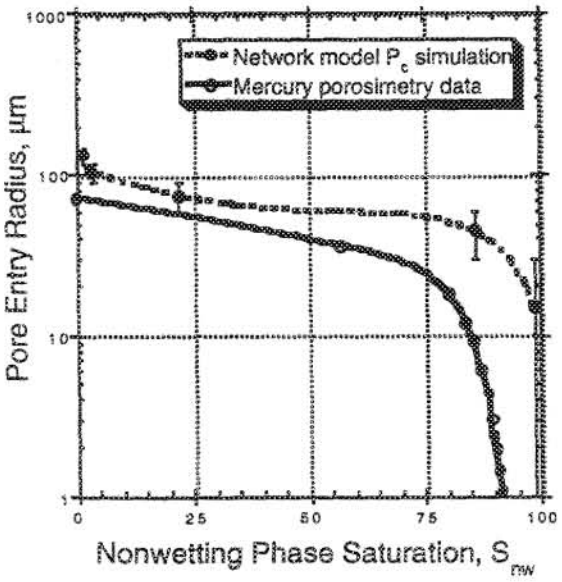

Figure 8. Simulated primary drainage in a CMT volume (ref 12), uncorrected for microporosity, compared with mercury intrusion data. Error bars indicate error range associated with thresholding the pore space. The same high permeability sample is represented in Figs. 5 & 6.

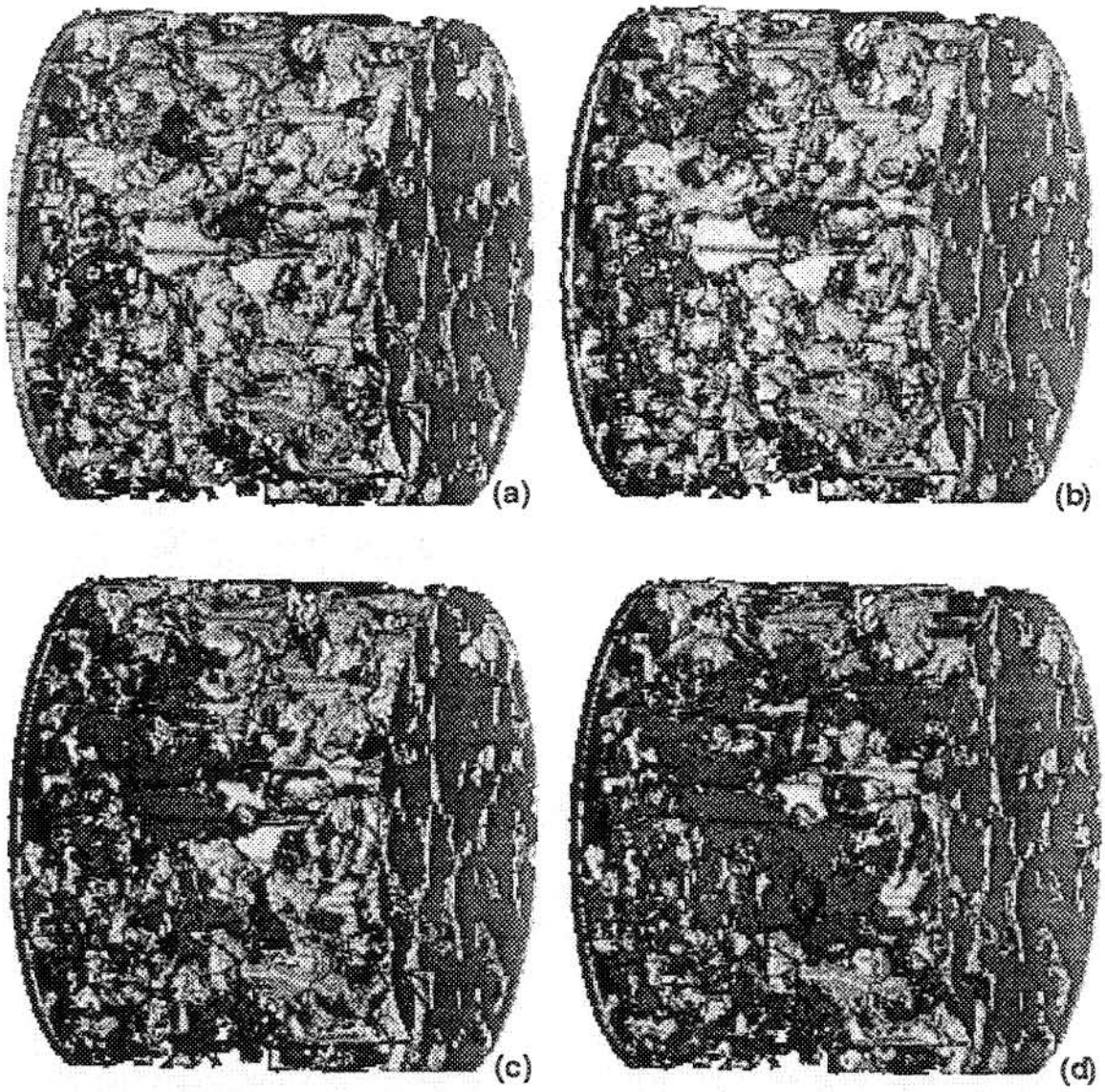

Figure 9. Snapshots of the saturation map during a simulated waterflood by the lattice Boltzmann method in a CMT volume from a producing sandstone reservoir (20 μm resolution; k = 7400 md). The rock is transparent. Light = Oil. Dark = Water. $N_{Ca} \sim 10^{-4}$. (a). Initial water saturation condition from network modeling, S_{iw} = 12%, (b). $S_w \sim 25\%$, (c). $S_w \sim 50\%$, (d) Simulation termination condition, S_{or} = 35%.